MONTE CARLO VARIATION OF SOLAR FLUX PROFILES AND DISPOSAL LIFETIME COMPLIANCE STATEGIES FOR GEOSYNCHRONOUS TRANSFER ORBITS

Juan C. Maldonado[(1)], Alan B. Jenkin[(1)], John P. McVey[(1)]

[(1)] *The Aerospace Corporation, P.O. Box 92957, Los Angeles, CA 90009-2957, USA, Emails:* *juan.c.maldonado@aero.org; alan.b.jenkin@aero.org; john.p.mcvey@aero.org*

ABSTRACT

Geosynchronous Transfer Orbits (GTOs) are becoming more widely used as mission orbits for small spacecraft that are rideshares on launches of primary spacecraft to geosynchronous Earth orbit. GTOs have the benefit of a low perigee so that atmospheric drag can enable reentry. However, meeting orbital lifetime limits in international debris mitigation practices is not straightforward due to a resonance that causes orbital lifetime of GTOs to be highly sensitive to solar cycle variations. This paper introduces a Monte Carlo methodology for modelling random variations in solar cycle parameters and using them in a propagation sweep to assess likelihood of compliance. Additionally, two mitigation strategies are considered: right ascension of ascending node interval targeting, and lowering perigee altitude via maneuvers. Results for a sample 6U CubeSat show that these mitigations increase percent compliance above the 90% threshold in international practices for a wide range of launch dates.

1 INTRODUCTION

Geosynchronous Transfer Orbits (GTOs) are orbits that have a perigee in low Earth orbit (LEO) and an apogee near geosynchronous Earth orbit (GEO). They are an intermediate orbit for launch missions to GEO between the upper stage apogee raising burn and the perigee raising burn. These types of orbits are becoming more widely used as mission orbits for small rideshare spacecraft that deploy into the GTO before the upper stage delivers the main payload to GEO. With the rate of small satellite launches rapidly growing around the world, it is expected that these rideshare opportunities will be increasingly utilized to enable affordable missions [1].

A GTO has the benefit of a perigee altitude that is low enough that atmospheric drag will reduce the orbital energy and enable an eventual atmospheric reentry of the spacecraft. A timely reentry is an important consideration for every mission designer due to restrictions on orbital lifetimes that are called out in international orbital debris mitigation guidelines. These must be assessed before launch to ensure that the spacecraft is promptly deorbited at the end of the mission and that it does not have an adverse effect on the space environment, especially since it will be passing through LEO, which is the most congested orbital regime. Additionally, spacecraft should be designed to demise during atmospheric reentry to avoid posing a serious threat to human populations on the ground as well as to global airline and maritime operations, especially if they will reenter in large numbers.

There are various debris mitigation guidelines that define the acceptable orbital lifetime. For example, the Inter Agency Space Debris Coordination committee (IADC) Space Debris Mitigation Guidelines [2] and the International Standards Organization (ISO) debris mitigation guidelines [3] both currently have a limit of 25 years on decaying disposal orbit lifetime. However, the U.S. Federal Communications Commission (FCC) has implemented a limit of 5 years [4].

To demonstrate compliance with deorbit duration requirements, mission planners will typically propagate out their intended disposal orbit using a high-fidelity propagator and show by analysis that their orbit meets the lifetime limit. However, this is not so simple to do for a GTO. It has been shown [5-7] that for GTOs, there exists a solar resonance phenomenon that results in a highly variable orbital lifetime for very small variations of the initial disposal orbit and other factors. The mechanism behind this begins with orbital perturbations due to Earth oblateness. As the apogee altitude decays, the nodal regression and apsidal rotation rates of the orbit increase due to Earth zonal harmonics. Eventually, integer combinations of the rates of right ascension of the ascending node (RAAN) and argument of perigee (AOP) (resonance angles) become synchronized with the rate of the argument of latitude of the Sun in its apparent orbit relative to the Earth. This causes the orbital eccentricity to undergo a large excursion during a limited period of time [5]. The direction and magnitude of the excursion is very sensitive to uncertainty in initial orbital elements, ballistic coefficient, and solar flux and geomagnetic activity.

Due to the variability of orbital lifetimes for GTOs and the inherent uncertainty behind the initial conditions known to affect the resonance, a probabilistic assessment must be performed to calculate the likelihood that an orbit will comply with a disposal rule across the possible

Proc. 9th European Conference on Space Debris, Bonn, Germany, 1–4 April 2025, published by the ESA Space Debris Office
Editors: S. Lemmens, T. Flohrer & F. Schmitz, (http://conference.sdo.esoc.esa.int, April 2025)

launch date range. This allows for launch dates and orbit configurations to be selected that show a probability of complying with the disposal rule above a specified threshold. The ISO debris mitigation guidelines [3] specify a threshold on likelihood of compliance of 90%. This reduces the risk of an unexpected long lifetime that might occur even though a single propagation of the mission orbit indicates a low orbital lifetime.

A Monte Carlo methodology for assessing likelihood of compliance for GTOs was presented by the authors in [8]. In that analysis, the authors did not yet have a capability to model random solar cycle variations, which affect atmospheric drag and hence long-term orbital propagations. Instead, the drag coefficient was randomly varied using a Gaussian spread as a surrogate.

Models of random solar cycle variations have been previously developed by other organizations. As an example, the CNES disposal orbit propagation tool STELA [9], which is used to assess compliance with the French Space Act [6], generates Monte Carlo variations of the solar cycle parameters for statistical assessment of orbital lifetime of resonant GTOs.

In this paper, a method to generate Monte Carlo variations of the solar flux and geomagnetic index profiles developed at The Aerospace Corporation is presented. In addition, two mitigation methods for increasing the likelihood of achieving compliant orbital lifetime are also presented, a RAAN interval targeting technique and a perigee altitude variation technique.

2 MONTE CARLO VARIATION OF SOLAR FLUX PROFILES

The Solar Prediction Generator (SPG) is a Python script that produces monthly solar flux and geomagnetic index predictions. The script requires two inputs: a NASA Marshall Space Flight Center (MSFC) solar cycle prediction file and historic solar cycle data files.

MSFC solar cycle predictions employ a statistical smoothing technique to estimate one cycle of solar fluxes and geomagnetic indices [10]. One could also consider using the Schatten solar flux prediction model used at Goddard Space Flight Center (GSFC) as a basis to perform this Monte Carlo variation [11]. However, this study uses MSFC predictions as its inputs. The MSFC solar cycle predictions file provides profiles of the 10.7 cm solar flux (F10.7) and geomagnetic index (Ap) at the 5^{th}, 50^{th}, and 95^{th} percentiles as a function of date, given in decimal years. Values are provided at one-month intervals.

The historic solar cycle data files provide past F10.7 and Ap values for six complete solar cycles and one partial solar cycle starting and ending at solar maxima.

The SPG solar cycle prediction is comprised of random draws of F10.7 and Ap values vs. time derived from the MSFC monthly predictions and a random selection of complete historic solar cycles appended to the end of the MSFC prediction time frame, extending the prediction to a user-selected date.

2.1 Random Solar Prediction over MSFC Prediction Time Frame

The SPG solar cycle prediction begins with the MSFC monthly solar cycle predictions. The MSFC percentile profiles extend through the next solar minimum. The percentile profiles contain little noise, instead capturing the overall shape and intensity of the upcoming solar cycle. Actual solar cycles have a significant random variation from month to month. To model this random variation, a Gaussian random variate U with zero mean (hence median) and unity standard deviation is generated and scaled to match the deviations of the MSFC 5^{th} and 95^{th} percentile profiles from the 50^{th} percentile profile. A random F10.7 or Ap is computed using Eqs. 1-2:

If $U \geq 0$,

$$G(t) = F_{50}(t) + \frac{F_{95}(t) - F_{50}(t)}{U_{95} - U_{50}} * (U - U_{50}) \qquad (1)$$

If $U < 0$,

$$G(t) = F_{50}(t) + \frac{F_{50}(t) - F_{5}(t)}{U_{50} - U_{5}} * (U - U_{50}) \qquad (2)$$

where:

$G(t)$ = random F10.7/Ap prediction

$F_5(t)$ = MSFC 5^{th} percentile F10.7/Ap prediction

$F_{50}(t)$ = MSFC 50^{th} percentile F10.7/Ap prediction

$F_{95}(t)$ = MSFC 95^{th} percentile F10.7/Ap prediction

U_5 = 5^{th} percentile, Gaussian (0, 1)

U_{50} = 50^{th} percentile, Gaussian (0, 1) (= 0)

U_{95} = 95^{th} percentile, Gaussian (0, 1)

U = random draw, Gaussian (0, 1)

Other than the three percentile levels, the MSFC monthly predictions file does not have any information on the distributions of F10.7 and Ap. Therefore, the model essentially assumes a two-sided Gaussian distribution.

It is noted that any correlation between the resulting *G(t)* values at different time points is due only to the MSFC profiles. Future work may investigate modelling any additional time-correlation on a shorter time scale in the historical solar cycles.

Figure 1 presents an example showing an F10.7 prediction from SPG over an MSFC prediction time frame.

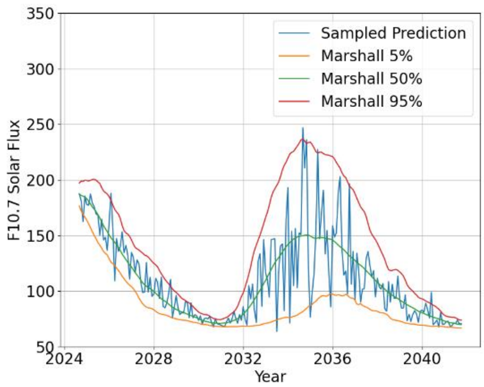

Figure 1. Sampled F10.7 prediction with MSFC predicted percentile profiles.

To check whether the SPG predictions represent the percentile profiles of the MSFC predictions, a Monte Carlo (MC) analysis was performed. SPG was used to generate 400 MC random profile predictions, and Figure 2 shows the resulting F10.7 profiles. Next, the 5th, 50th, and 95th percentile levels were computed from the 400 MC random profile predictions at each monthly interval. Figures 3-4 show that these percentile levels from the MC profiles closely track the corresponding percentile levels from the MSFC prediction.

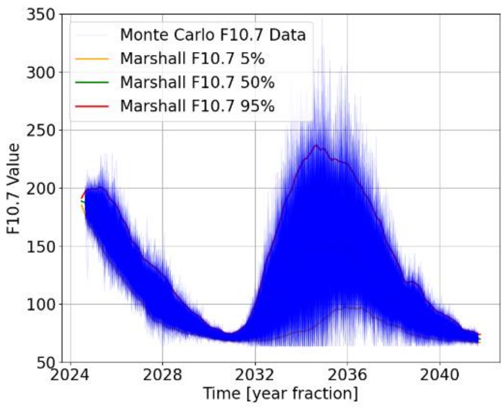

Figure 2. 400 MC sampled F10.7 predictions.

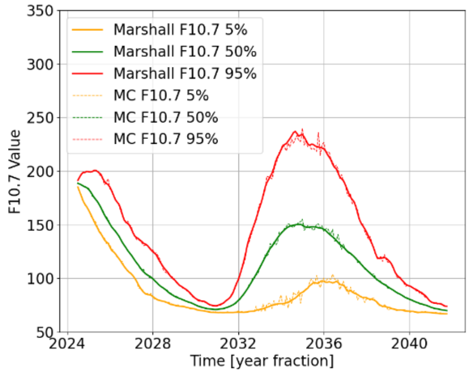

Figure 3. MC F10.7 percentiles with MSFC percentiles.

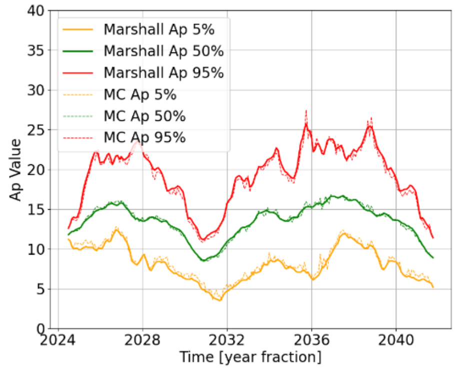

Figure 4. MC Ap percentiles with MSFC percentiles.

2.2 Appending Historical Solar Cycles

The historic solar cycle data currently available consists of six full cycles spanning solar maximum to solar maximum and one partial cycle starting at solar maximum and continuing to solar minimum. Figures 5 and 6 show the historical values of F10.7 and Ap, respectively, through January 3, 2023.

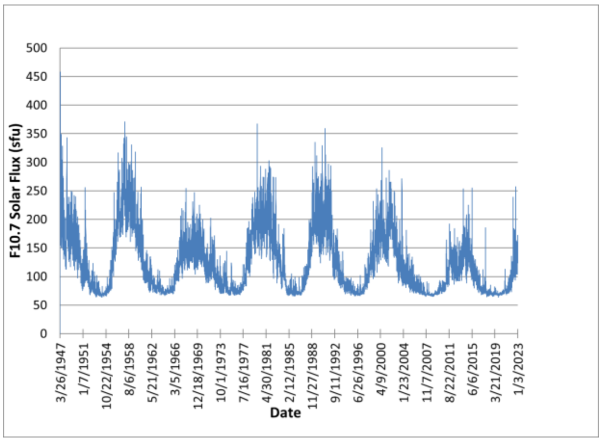

Figure 5. Historical values of F10.7. Source of data: NOAA [12].

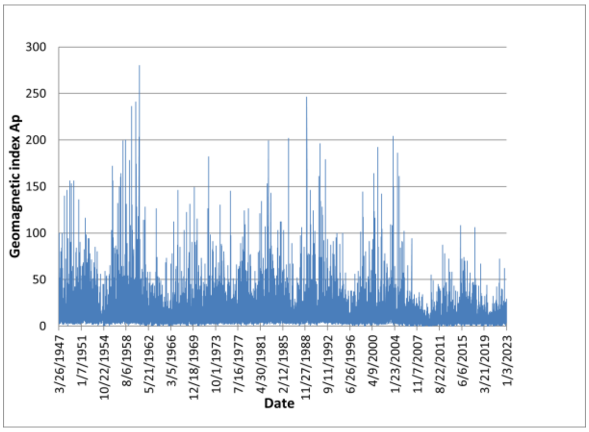

Figure 6. Historical values of Ap. Source of data: NOAA [12].

The MSFC solar cycle prediction ends at a solar minimum, which requires the historic solar cycle data to be sliced such that each cycle starts and ends at solar minimum. Additionally, solar minimum has the most consistent magnitude across all solar cycles resulting in strong alignment when appending cycles randomly.

To provide future solar cycles starting and ending at solar minima, solar cycles are randomly selected. The end of each cycle (ending at solar minimum) is paired with the start of the next cycle (starting at solar minimum). Ultimately, the start of Cycle One is discarded and the partial Cycle Seven is utilized, paired with the end of Cycle Six. As examples, the first sliced F10.7 solar cycle and Ap solar cycle available for random draw are shown in Figs. 7-8, respectively.

The CNES disposal orbit propagation tool STELA [9] also performs a similar random selection of historical solar cycles in its statistical analysis mode.

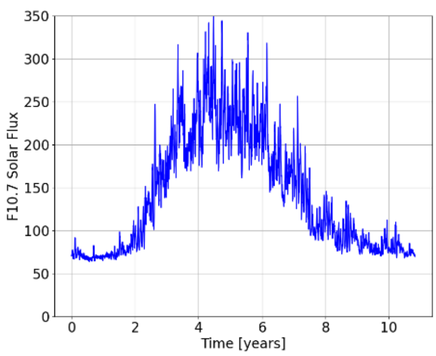

Figure 7. F10.7 for Solar Cycle 1.

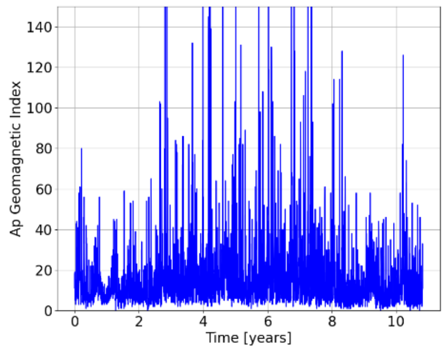

Figure 8. Ap for Solar Cycle 1.

Figure 9 shows the MSFC-based F10.7 prediction from Fig. 1 with randomly selected historical F10.7 cycles appended to extend the prediction approximately 55 years beyond the end of the MSFC prediction time frame. Figure 10 shows a similar plot for Ap. The data in Figs. 9-10 is at one-month intervals, whereas the data in Figs. 5-8 is at one-day intervals. It is noted that the MSFC-based Ap prediction portion of the entire predicted profile does not have spikes, but the historical-cycle based portion does have spikes. This can be attributed to the source data, in which the historical Ap cycle data has spikes, whereas the MSFC percentile profiles do not contain any spikes.

The advantage of this methodology is that it utilizes the prediction information embedded in the MSFC profiles but also allows for an extension beyond the MSFC prediction range so that the effect on orbital evolution over longer time frames can be modelled.

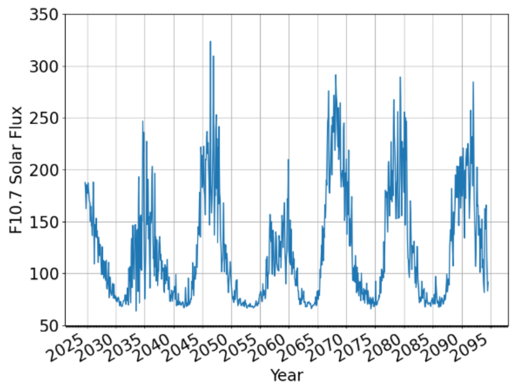

Figure 9. Extended sampled F10.7 prediction.

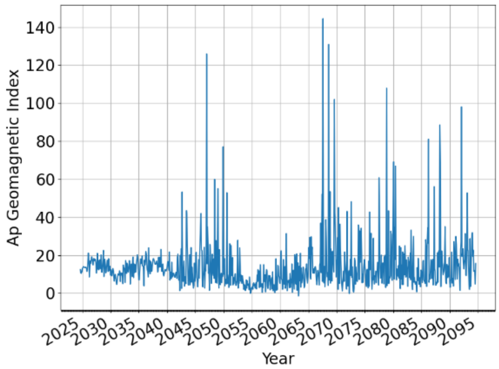

Figure 10. Extended Sampled Ap prediction.

3 SIMULATION SETUP

The methodology used for the simulations is based on that presented in [8] and considered 400 MC initial condition vectors generated for each date in a launch date range. The initial conditions are propagated for 100 years, or until reentry, which in the propagations was triggered when the altitude fell below 110 km. For the MC initial condition vectors, the RAAN was uniformly randomly varied from 0 to 360 degrees. In contrast to the method in [8], in this study the drag coefficient, C_d, was set to a constant value of 2.1, which is the value for a tumbling plate [13-14]. An assumption of this study is that this value can be roughly applied to the 6U CubeSat considered in the analysis. The mass and area for the CubeSat, shown in Table 1, were fixed in the propagations.

Table 1. 6U CubeSat Physical Properties

Mass (kg)	10
Mean projected area (m^2)	0.085
Area-to-mass ratio (m^2/kg)	0.0085

The F10.7 and Ap data used for the simulations were generated using the process presented in Section 2 to create 400 distinct F10.7/Ap data files based on the NASA MSFC monthly predictions posted on January 2025 [15]. These files were used in the propagations for the corresponding MC group of the initial condition vectors, e.g., the initial condition vectors corresponding to MC #1 at each launch date were propagated using the MC #1 F10.7/Ap prediction data file.

The considered launch date range spanned 90 days from 2025-1-1 to 2025-3-31. The analysis generated 400 MC initial condition vectors per launch date, yielding a total of 36,000 initial condition vectors.

For comparison, 400 MC simulations using the drag variation methodology presented in [8] were performed. The same initial condition vectors used for the MC variation of F10.7 and Ap were selected, but instead of randomly varying F10.7 and Ap, the C_d was randomly varied for each MC using a Gaussian distribution with a mean value of 2.1 and 3-sigma variation of 0.1. The 50th percentiles of F10.7 and Ap from the MSFC data, posted on January 2025, were used for the propagations. This prediction ends in October 2041 and was extended past that date by repeating the pattern of the last 11 years to enable the 100-year propagation times. A summary of the initial condition vectors is shown in Table 2.

The precision integration tool TRACE, developed by The Aerospace Corporation, was used for the orbital lifetime propagations [16]. The runs included atmospheric drag computed from the MSISE-2000 atmosphere model, a 70 x 70 modified WGS84 Earth gravity model, Sun and Moon gravity, and solar radiation pressure (assumed reflectivity coefficient of 1.3). For the computation of the Sun and Moon perturbations, the Sun and Moon ephemerides were generated using an implementation of an analytical model by Fliegel and Harrington [17]. For the Sun, the model uses the theory of motion by Newcomb [18]. For the Moon, the model uses the theory of Brown modified with improved values of fundamental constants by Eckert et al. [19]. The model also uses the International Astronomical Union 1980 Theory of Nutation [20]. For numerical integration, TRACE uses an 8th order Cowell second-sum method, otherwise known as the Gaussian Jackson method, with a Runge-Kutta starter [21].

The inputs for TRACE are the MC initial condition vectors described in Table 2 with the constant spacecraft information from Table 1. Each of the runs produces an osculating orbital element ephemeris file that goes from the specified launch date until either a reentry occurs, or a 100-year propagation is reached. To make the turn-around time acceptable, the TRACE runs were implemented on The Aerospace Corporation's computing cluster.

Table 2. MC Simulation Inputs

400 MC Cases per Launch Day from 2025-1-1 to 2025-3-31						
Perigee / Apogee Altitude (km)	Eccentricity	Inclination (deg)	RAAN (deg)	Argument of Perigee (deg)	Mean Anomaly (deg)	C_d

185 / 35,786	0.73	23	Varied from 0 to 360 deg	180	0	**For MC F10.7/Ap run**: 2.1 (constant) **For comparison run using methodology in [8]:** **Gaussian C_d**: 2.1±0.1 (3-sigma)

4 ATMOSPHERIC VARIATION MODELLING COMPARISON

Figs. 11-12 show the orbital lifetime compliance behavior across the launch date range for both methods of atmospheric variation modelling when evaluated against a 25 and a 5-year deorbit rule. The compliance profiles were created by determining the percentage of MC propagations that had a lifetime less than or equal to 25 years, or 5 years, on each launch date. Note that the compliance behavior changes rapidly across the launch date range, which is a consequence of the solar resonance and its dependence on the positions of the Sun and Moon relative to the spacecraft orbit. Also note that in Fig. 11, only portions of the launch date range have a probability of compliance greater than or equal to 90%, which is the desired threshold commonly used in practice and consistent with the IADC and ISO guidelines. Fig. 12 shows that the entire launch date range is below the 90% threshold, which suggests that an alternative method may be required to enable compliance with a 5-year rule.

The blue solid line in the figures corresponds to the propagation that had a fixed C_d and utilized the MC F10.7/Ap data generated using the process detailed in Section 2. The orange dashed line corresponds to the propagation that utilized a Gaussian distribution on the C_d and considered the same F10.7/Ap data for all MC initial condition vectors. The results show close agreement between the two methods of atmospheric variation modelling, with the main compliance behavior being captured even when using the Gaussian C_d method. This suggests that the variability of the orbital evolution of the GTO cases is dominated by the exponential variation in drag with perigee altitude variations during the resonances rather than by the variation in drag force over time due to either atmospheric density variations or random C_d variation. In [8] the Gaussian C_d variation method was used as a simple surrogate due to lack of a model of F10.7 and Ap variation, but it is not considered a representation of reality as C_d depends on both object shape and altitude in the atmosphere. For orbits that are not subjected to the resonance and where atmospheric variations over time have a more direct impact on the orbital evolution, such as for a spacecraft in LEO, the MC F10.7/Ap method is expected to be a better representation of reality. Therefore, the MC F10.7/Ap modelling method is recommended in general instead of the Gaussian C_d variation method. A study of the MC F10.7/Ap modelling method across a range of orbits is left as a topic for a future paper.

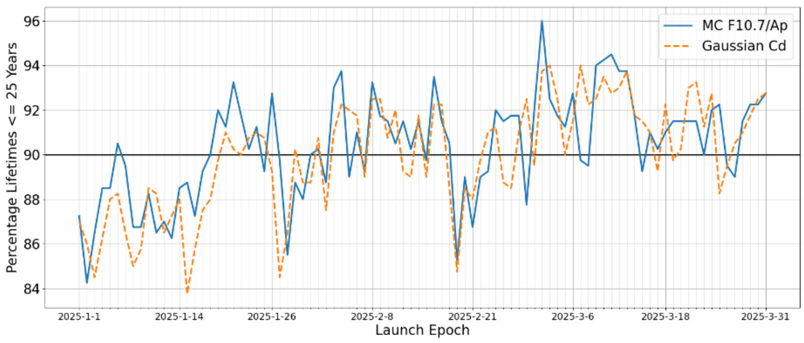

Figure 11. Drag modelling comparison: 25-year orbital lifetime compliance behaviour.

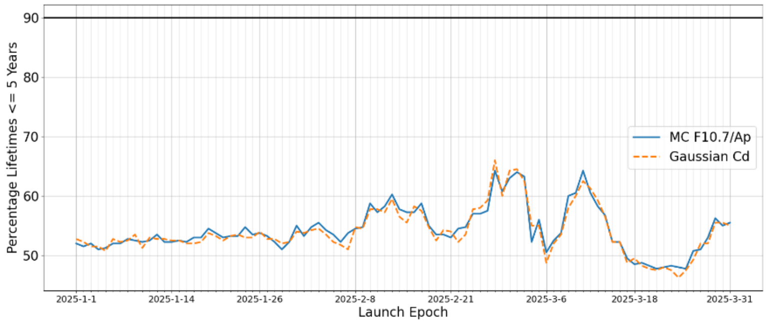

Figure 12. Drag modelling comparison: 5-year orbital lifetime compliance behaviour.

5 COMPLIANCE TECHNIQUES

One method to help improve the compliance performance would be to use a drag enhancement device to quicken deorbit, as discussed in [8]. That analysis also showed that the associated increased area magnifies the effect of solar radiation pressure, which can increase the solar resonance effect and work against increasing percent compliance.

In this paper, two alternative mitigation techniques are considered: a RAAN interval targeting technique and a perigee altitude variation technique.

5.1 RAAN Interval Targeting

The mechanism by which the solar resonance affects the orbital lifetime is an eccentricity excursion which occurs when certain combinations of the RAAN and the AOP (the resonance angles) become synchronized with the rate of the argument of latitude of the Sun in its apparent orbit relative to the Earth [5,8]. The location of the Sun with respect to the orbit is driven by the insertion RAAN on a given launch date. Therefore, the initial RAAN can constrain when the spacecraft passes through the resonance region, i.e., when the resonance angles become synchronized, as is shown in Fig. 13. The insertion RAAN is controlled by the launch time on a given day. In practice both may be driven by mission constraints. If there are no constraints on launch time, then RAAN selection could be used to improve compliance.

As discussed in [7, 22-24], lunisolar perturbations introduce long-period and short-period oscillations on the perigee altitude for GTOs. This perigee altitude oscillation behavior presents a method to decrease the orbital lifetime, whereby if the phasing on the long-period perigee altitude oscillation is near the peak at the start of the deorbit, the perigee altitude will then be decreasing on the oscillation curve during the initial deorbit [7, 22-24]. This means that the spacecraft will be experiencing a higher drag force and can deorbit quicker. If the converse is true, then the spacecraft will be experiencing a lower drag force during the initial trajectory and will deorbit slower. The phasing on the perigee altitude oscillation can also be changed by selecting the initial RAAN, as discussed in [23].

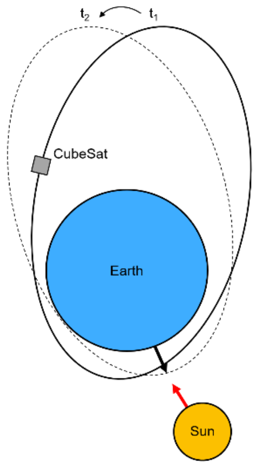

Figure 13. J_2 Effect on orbit rotation and aligning with resonance configuration.

To study the interplay between the solar resonance and the perigee altitude oscillation behavior, a similar Monte Carlo analysis was conducted as in Section 3 except that this time the random uniform RAAN distribution was constrained to be within 30 deg RAAN intervals for the MC initial condition vectors. This resulted in 12 separate Monte Carlo analyses covering RAAN intervals from 0 to 30 deg, 30 to 60 deg, 60 to 90 deg, etc.

Figs. 14-19 show the results of this analysis for compliance with a 25 and 5-year rule. The plots are in the form of grids over the launch date range, where the 400 MC initial condition vectors per launch date are evaluated at each grid point for each of the considered RAAN interval cases. Fig. 14 and Fig. 17 show a binary grid across all RAAN intervals, where the yellow grids (or the grids with the letter "C") correspond to the MC initial condition vectors that had a percent compliance greater than or equal to 90%. Figs. 15-16 and Figs. 18-19 show a color mapped grid that corresponds to the percent compliance across the MC initial condition vectors on each launch date, with the value for the specific percent compliance contained in the grids. The results show that there are RAAN intervals with significantly better compliance performance, such as the RAAN interval range from 180-210 deg. There are also RAAN intervals with poor performance, such as the range from 300-330 deg. From a mission perspective, it is evident that constraining the insertion RAAN to a specific range can be a powerful tool for improving compliance versus leaving the RAAN open to any value, as was done in Figs. 11-12.

To understand why certain RAAN ranges result in starkly different orbital lifetimes, the perigee altitude evolution and resonance angle rate plots can be inspected. Fig. 20 shows the apogee and perigee altitude evolution for MC initial condition vector number 15202 on 2025-2-8 for the 300-330 deg RAAN interval case. Fig. 21 shows a zoomed in plot on the perigee altitude evolution and Fig. 22 shows the corresponding resonance angle rates. The rates of the resonance angles (defined in [5]) were computed by using a finite difference method applied to the AOP and RAAN data obtained from the TRACE propagations. When the resonance angle rates are in sync with the rate of the Sun Mean Right Ascension, then the resonance occurs.

In Fig. 20, a levelling of the apogee altitude around 20 years into the simulation can be seen, which is indicative of the resonance affecting the orbit. In Fig 21, the typical short period oscillations for the GTO perigee altitude are observed at the beginning of the deorbit. The lowest excursion of perigee altitude is down to approximately 200 km. Then, a drastic increase in the perigee altitude is seen followed by the levelling of the perigee altitude oscillation at a higher altitude. This rapid increase coincides to when the rate of AOP + RAAN lines up with the rate of the Sun Mean Right Ascension in Fig. 22. At an inclination of about 23 deg, this configuration can be physically interpreted as occurring when the disposal orbit perigee vector begins tracking the Sun vector, as depicted in Fig. 13. This orbit was highly perturbed by the solar resonance since the phasing on the perigee altitude oscillation was such that it was at a high point when passing through the resonance region, meaning that the lower drag force was not able to dampen the effect of the resonance, and the eccentricity decreased (increase in perigee altitude).

Looking now at the 180-210 deg RAAN interval data on 2025-3-26 (specifically, looking at MC initial condition vector number 33601), which had high compliance performance across the entire launch date range, it is seen that the apogee/perigee altitude oscillation looks completely different. Now, in Fig. 23, the apogee altitude does not exhibit the levelling behaviour indicative of the resonance. Looking at Fig. 24 for the zoomed in perigee altitude, it can be seen that the perigee altitude moves downward well below 200 km and does not have a sudden increase like in Fig. 21. The resulting orbital lifetime is only slightly over one year. Looking at Fig. 25, it is evident that no resonance is occurring when the corresponding resonance angle rates cross the rate of the Sun Mean Right Ascension. Thus, this case of short deorbit lifetime is attributed to the phasing on the perigee altitude oscillation. The perigee altitude starts at a high point on the oscillation curve and moves downward, leading to a faster deorbit.

The results in this section showcase how constraining the RAAN can enable significant improvements to the probability of being compliant with a 25 and 5-year rule across a launch date range. The results show that certain RAANs are predisposed to longer lifetimes (or shorter lifetimes) due to the phasing on the perigee altitude oscillation curve and the timing of the solar resonance.

5.2 Perigee Altitude Variation

Another method to improve the probability of complying with deorbit rules for decaying GTOs is to perform a maneuver to lower the perigee altitude of the orbit. This will result in the spacecraft experiencing a higher drag force during the perigee passes, which will help speed up deorbit and improve compliance performance.

To study this, two sets of MC initial condition vectors were generated based on those listed in Table 2 (considering the 0-360 deg RAAN spread) except that perigee altitude was lowered below the reference perigee altitude of 185 km. The first set had a perigee altitude of 165 km, which will require a maneuver delta-V of 2.1 m/s The second set had a perigee altitude of 145 km, which will require a delta-V of 4.2 m/s. The delta-Vs were computed from the vis-viva orbital energy equation and assume impulsive maneuvers, i.e., no losses were modelled. These delta-V levels would be achievable by a simple hot steam propulsion system on a CubeSat. The results of this analysis are shown in Fig. 26-27. Note that the blue solid line labelled as “No maneuver” is the same data shown in Figs. 11-12 generated using the MC F10.7/Ap method.

Figs. 26-27 show that implementing a maneuver to lower the perigee did improve the compliance performance across the entire launch date range. Percent compliance with the 25-year limit is above the 90% threshold for both lowered perigee altitude cases for the entire launch date range. There are even portions of the launch date range that percent compliance with the 5-year rule is above 90% for the 145 km perigee altitude case. The overall profiles look similar due to how the RAAN distribution across the MC initial condition vectors was the same, so the propagations were similarly affected by the solar resonance and also had the same initial phasing on the perigee altitude oscillation curve.

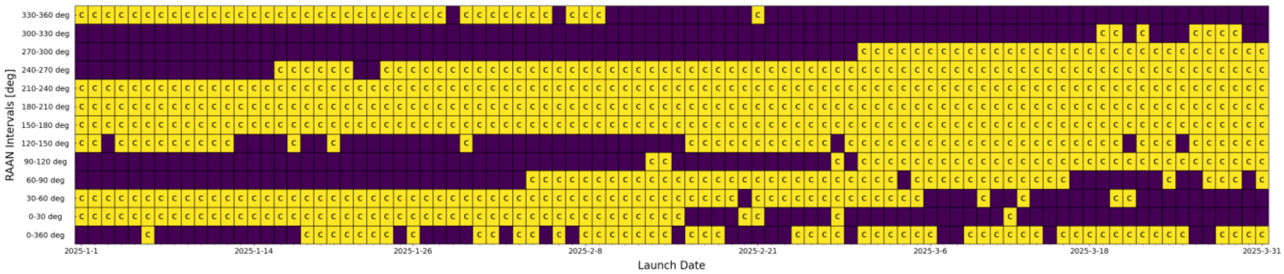

Figure 14. 25-year orbital lifetime compliance: binary grid.

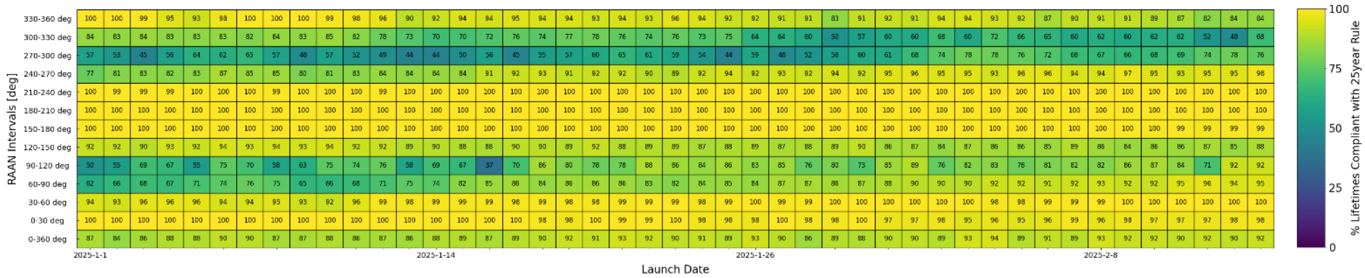

Figure 15. 25-year orbital lifetime compliance: percent compliance grid from 2025-1-1 to 2025-2-14.

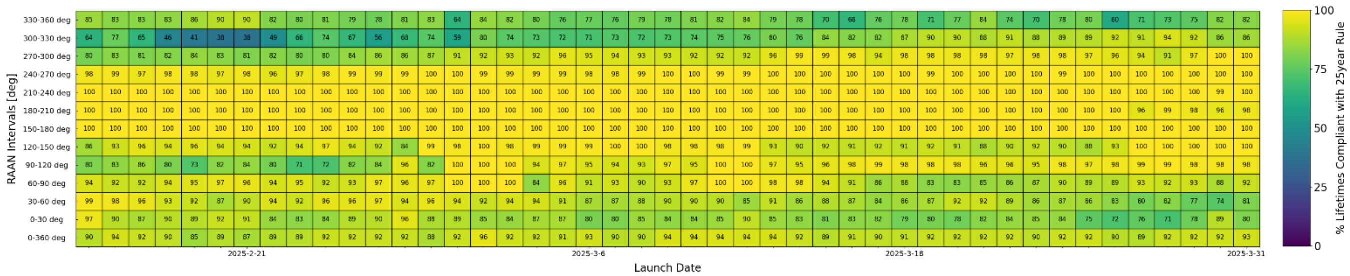

Figure 16. 25-year orbital lifetime compliance: percent compliance grid from 2025-2-15 to 2025-3-31.

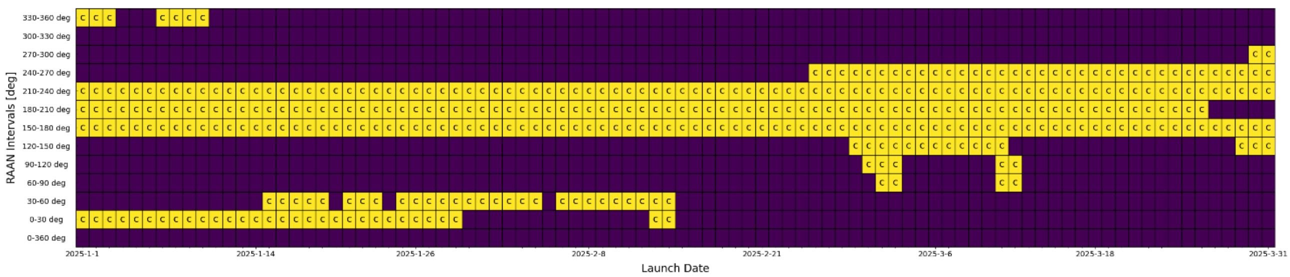

Figure 17. 5-year orbital lifetime compliance: binary grid.

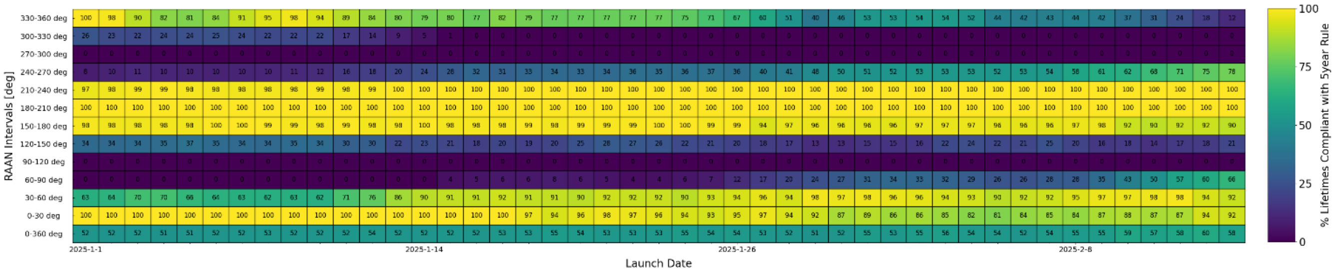

Figure 18. 5-year orbital lifetime compliance: percent compliance grid from 2025-1-1 to 2025-2-14.

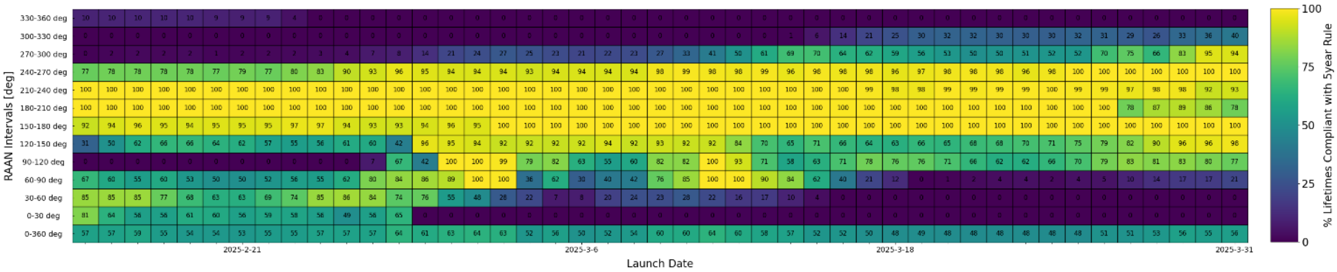

Figure 19. 5-year orbital lifetime compliance: percent compliance grid from 2025-2-15 to 2025-3-31.

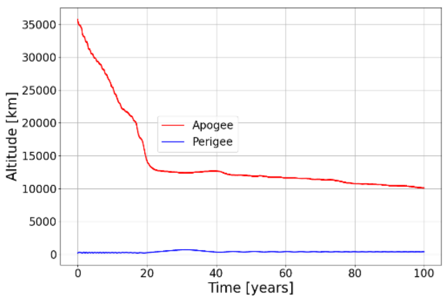

Figure 20. Apogee/perigee altitude evolution for MC vector on 2025-2-8: 300-330 deg RAAN interval case.

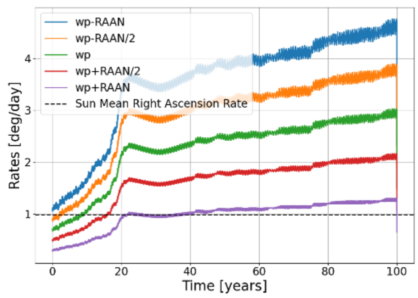

Figure 22. Resonance angle rate evolution for MC vector on 2025-2-8: 300-330 deg RAAN interval case.

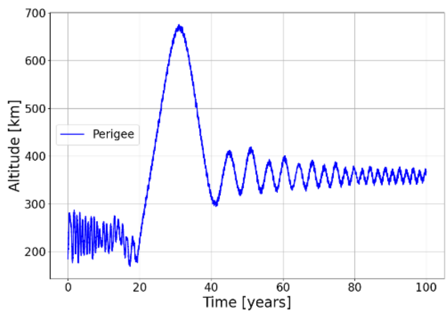

Figure 21. Zoomed in perigee altitude evolution for MC vector on 2025-2-8: 300-330 deg RAAN interval case.

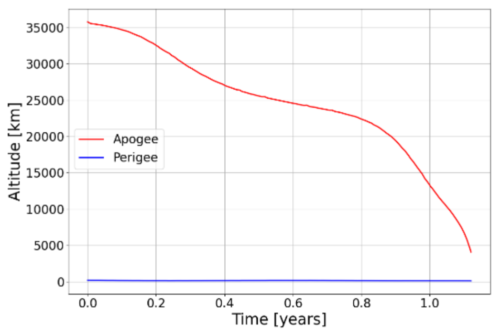

Figure 23. Apogee/perigee altitude evolution for MC vector on 2025-3-26: 180-210 deg RAAN interval case.

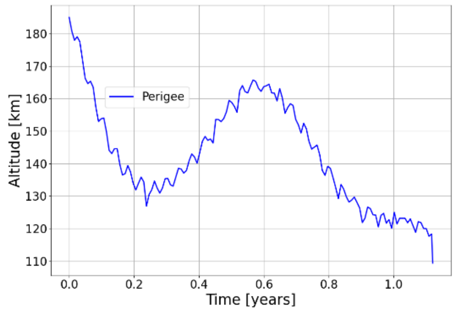

Figure 24. Zoomed in perigee altitude evolution for MC vector on 2025-3-26: 180-210 deg RAAN interval case.

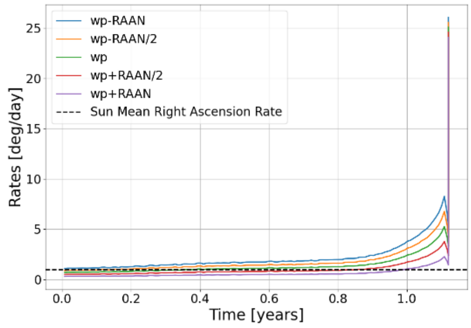

Figure 25. Resonance angle rate evolution for MC vector on 2025-3-26: 180-210 deg RAAN interval case.

However, the peaks and dips are smoothed out as the perigee altitude is lowered, suggesting that lowering the perigee altitude has the effect of providing dampening against the solar resonance, helping to provide more consistent compliance performance. Another effect that is observed is that lowering the perigee altitude results in an upwards shift of the compliance profile, with more MC initial condition vectors now having compliant deorbits. This could be due to the faster overall decay of the orbits as well as to an increased robustness against the resonance from the larger drag force during the perigee passes.

The results in this section demonstrate how performing a maneuver to lower the perigee altitude can help to increase the probability of compliance across a launch date range. The benefits of lowering the perigee altitude are not as pronounced as those obtained when constraining the RAAN interval, however, this method offers a beneficial alternative to missions that are not able to constrain the insertion RAAN and would like to have a high probability of compliance across the full 0-360 deg RAAN range.

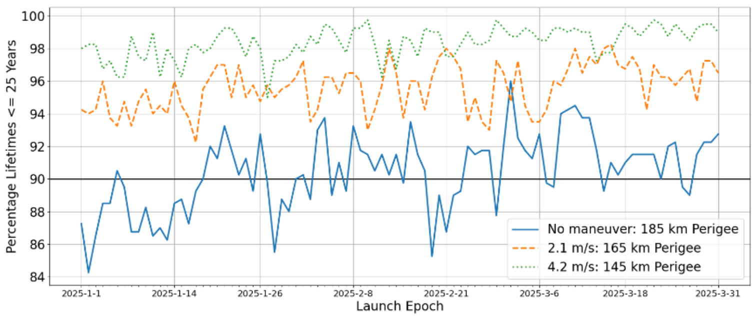

Figure 26. Perigee altitude variation modelling comparison: 25-year orbital lifetime compliance behaviour.

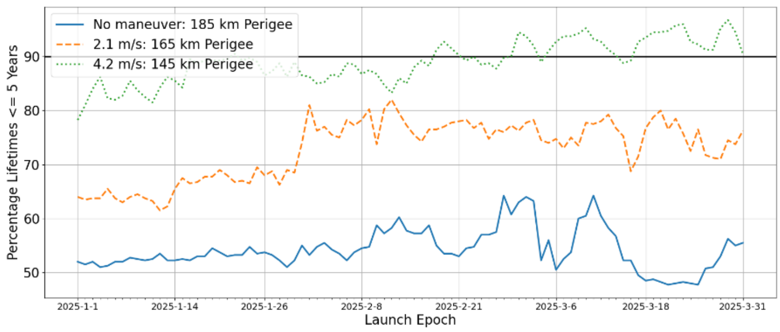

Figure 27. Perigee variation modelling comparison: 5-year orbital lifetime compliance behaviour.

6 CONCLUSIONS

This paper presented a methodology for improving the fidelity of atmospheric variation modelling in long-duration propagations to generate MC F10.7/Ap profiles based on the NASA MSFC monthly predictions. These MC F10.7/Ap profiles were incorporated into the MC propagation methodology presented in [8] to generate compliance profiles for a 25 and 5-year deorbit rule across a launch date range. Two methods for improving the compliance performance were also presented, a RAAN interval targeting technique and a perigee altitude variation technique. Results showed that the RAAN interval targeting technique can help to significantly improve the compliance performance by selecting an orbit that is predisposed to faster deorbit times due to the phasing on the perigee altitude oscillation curve. Results also showed that certain insertion RAANs conversely lead to significantly longer lifetimes due to the solar resonance and the interplay with the phasing on the perigee altitude oscillation. The perigee altitude variation technique offers a beneficial alternative that can help improve the compliance performance across the full 0-360 deg RAAN range, which can be useful for missions that are not able to constrain their insertion RAAN. Results showed that by performing a maneuver to lower the perigee altitude, the lifetimes are shortened on average due to the higher drag force, and fluctuations on the compliance profile due to the solar resonance are smoothed out since the higher drag force now offers increased robustness to the resonance.

7 ACKNOWLEDGMENTS

This work reflects research conducted under U.S. Space Force Space Systems Command (SSC) Contract FA8802-09-C-0001. The authors wish to thank several individuals and organizations for their support of this work and assistance in preparing this paper. Jack Toland developed the Solar Prediction Generator while an intern at The Aerospace Corporation in summer 2019. The description of the SPG methodology in this paper used much of the text in his Aerospace Technical Memorandum with modifications to reflect further development by the authors. Technical committee members Marlon Sorge, Glenn Peterson, and Sam Peresztegy provided technical review of the paper. Sam Peresztegy provided Aerospace programmatic support for this work. The Space Debris Management Office in SSC/BZES provided support for the study presented in this paper. The Aerospace Corporation's Office of Technical Relations provided publication clearance review.

8 REFERENCES

1. Villela, C.A. Costa, A.M. Brandão, F.T. Bueno, R. Leonardi, Towards the thousandth CubeSat: a statistical overview, International Journal of Aerospace Engineering 2019 (2019).
2. Inter-Agency Space Debris Coordination Committee, Space Debris Mitigation Guidelines, www.iadc-home.org/documents_public/index.
3. ISO 24113, Space Systems – Space Debris Mitigation Requirements, Fourth Edition, 2023-05.
4. W. Wiquist, FCC Adopts New '5-Year Rule' for Deorbiting Satellites to Address Growing Risk of Orbital Debris, 2022 https://docs.fcc.gov/public/attachments/DOC-387720A1.pdf
5. A.B. Jenkin, J.P. McVey, B.D. Howard, Uncertainty in lifetime of highly eccentric transfer orbits due to solar resonances, Paper No. AAS 11-597, Advances in the Astronautical Sciences 142 (2012) Astrodynamics 2011.
6. H. Fraysse, C. Le Fèvre, V. Morand, A. Lamy, D.A. Handschuh, Statistical methods to address the compliance of GTO with the French Space Operations Act, 2013 Paper No. IAC-13,A6.4,3x19616, 64th International Astronautical Congress, Beijing, China, Sept. 23-27.
7. A. Lamy, C. Le Fevre, B. Sarli, Analysis of geostationary transfer orbit long term evolution and lifetime, Journal of Aerospace Engineering Sciences and Applications (2012).
8. J.C. Maldonado, A.B. Jenkin, J.P. McVey, Probabilistic assessment of disposal orbit lifetime for CubeSat rideshares on resonance decaying geosynchronous transfer orbits, Journal of Space Safety Engineering 2024.
9. CNES STELA User's Guide Version 3.4, 2021 https://www.connectbycnes.fr/sites/default/files/2022-03/V3.4%20Stela-User-Manual_0.pdf.
10. W.W. Vaughan, J.K. Owens, K.O. Niehuss, M.A. Shea, The NASA Marshall solar activity model for use in predicting satellite lifetime, Advances in Space Research, Volume 23, Issue 4, 1999, Pages 715-719, ISSN 0273-1177, https://doi.org/10.1016/S0273-1177(99)00140-4.
11. Schatten Solar Flux Files, https://ai-solutions.com/_help_Files/schatten_solar_flux_files.htm.
12. NOAA Space Weather Prediction Center, https://www.swpc.noaa.gov/products-and-data.
13. H. Fraysse, V. Morand, C.Le Fevre, F. Deleflie, S. Wailliez, A. Lamy, T. Martin, E. Perot, Long term orbit propagation techniques developed in the frame of the French Space Act, in: Proceedings of the 5th IAASS Conference, European Space Agency, Noordwijk, Netherlands, 2012 id.89January 2012.

14. K. Moe, M.M. Moe, Gas-surface interactions and satellite drag coefficients, Planetary and Space Science 53 (2005) 1515.
15. NASA Marshall Solar Radio Flux Extended Forecast, 2025 https://www.nasa.gov/solar-cycle-progression-and-forecast/.
16. W.D. Downs III, R.H. Prislin, D.C. Walker, R.J. Mercer, TRACE trajectory analysis and orbit determination program, 1974 The Aerospace Corporation Report SAMSO-TR-71-141.
17. H.F. Fliegel, K.M. Harrington, Closed form sun, moon, and nutation algorithms: applications for TRACE and the Global Positioning System, 1993 Aerospace Report No. ATR-93(3473)-1.
18. S. Newcomb, Astronomical papers prepared for the use of the American ephemeris and Nautical Almanac, U. S. Naval Observatory, Washington DC, 6, 1898 171ff.
19. W.J. Eckert, R. Jones, H.K. Clark, Construction of the lunar ephemeris, Improved Lunar Ephemeris 1952-1959, US Naval Observatory, 1954, pp. 283–363. Washington DC.
20. J.M. Wahr, Geophysical journal of the Royal Astronomical Society 64 (1981) 705–727.
21. J.F. Holt, Floating point Cowell (second-sum), Runge-Kutta integration of Second-order ordinary differential equations (subroutine ASC DEQ4), The Aerospace Corporation, 1968.
22. K.H. Siebold, R.C. Reynolds, Lifetime Reduction of a Geosynchronous Transfer Orbit with the Help of Lunar-Solar Perturbations, Advances in Space Research, Volume 16, Issue 11, 1995.
23. Y. Wang, P. Gurfil, Dynamical modelling and lifetime analysis of geostationary orbits, Acta Astronautica 2016.
24. G. Janin, Lifetime of Objects in Geostationary Transfer Orbit, European Space Operations Centre, Mission Analysis Section, Proc. Internat. Workshop on Salyut-7 / Kosmos-1686 Reentry, ESOC, Darmstadt (D), 9 April 1991.